*13,16*

# Structural and electronic properties of composite memristors based on the $LiNbO_3$ 3 matrix with different nanogranules: Co–Fe–B and CoFe

© *K.Yu. Chernoglazov*[1], *R.G. Chumakov*[1], *E.V. Khramov*[1], *K.E. Nikiruy*[1], *A.V. Sitnikov*[1,2], *V.A. Demin*[1], *E.M. Pashaev*[1], *V.V. Rylkov*[1,3]

[1] National Research Center „Kurchatov Institute“,
Moscow, Russia
[2] Voronezh State Technical University,
Voronezh, Russia
[3] Fryazino Branch, Kotel'nikov Institute of Radio Engineering and Electronics, Russian Academy of Sciences,
Fryazino, Moscow oblast, Russia
E-mail: expe28@gmail.com

*Received June 21, 2023*
*Revised June 21, 2023*
*Accepted June 22, 2023*

Comparative studies of the properties of metal/nanocomposite/metal (M/NC/M) memristive structures based on NC consisting of a $LiNbO_3$ matrix and various Co–Fe–B or CoFe metal granules have been carried out. The M/NC/M structures were obtained using ion-beam sputtering from composite targets $Co_{40}Fe_{40}B_{20}$-$LiNbO_3$ and $Co_{50}Fe_{50}$-$LiNbO_3$ on glass-ceramic substrates. The same NC layers were synthesized on polyimide substrates to study the structural features by X-ray absorption fine structure spectroscopy (XAFS). The XAFS data show an identical crystal structure of granules in both types of NC, indicating that a significant part of the B atoms during the synthesis of NC is in an insulating matrix, forming an oxide of the $B_2O_3$, which is confirmed by X-ray photoelectron spectroscopy data. In this case, no metallic state of niobium is observed in the layers. Both types of M/NC/M structures demonstrate resistive switching (RS), however, in the case of NC with boron, the RS effect is much stronger, which is explained by the significant role of oxygen vacancies formed during the oxidation of boron in the RS.

**Keywords:** memristors, metal-dielectric nanocomposites, resistive switching, neuromorphic systems, synchrotron light source, XAFS, XPS.

DOI: 10.61011/PSS.2023.09.57121.118

## 1. Introduction

Currently, there is a keen interest in studying metal-insulator-metal (MIM) memristive structures that demonstrate reversible resistive switching (RS) effects in connection with future application in production of matrix-type multilevel memory cells and memristor arrays simulating synapses in neuromorphic computer systems (NCS) designed to address artificial intelligence tasks [1–4].

RS effects in the MIM structures are generally attributable to electromigration of oxygen vacancies (anions)or metal cations [1–3]. As a result, filamentary conducting channels (filaments/bridges) are formed (or broken) in the dielectric (oxide) layer, and the structure is switched to low-resistance state (LRS) or high-resistance (HRS), respectively. Filament formation is to a great extent random in nature, which is one of the root causes of MIM memristor degradation in cyclic RS [1,2]. Though other type („non-filament“) of memristors is known currently (e.g. based on the phase transition between the amorphous and crystalline states of a material or ferroelectric repolarization in dielectric [1,3]), of utmost interest are still oxide (ionic) MIM-structures as the systems that may have multilevel RS with long resistive state storage times and are also production-friendly and can be easily integrated into the up-to-date microelectronic technology [1,2,5].

We have lately found and investigated the multilevel RS effects in metal/nanocomposite/metal (M/NC/M) structures based on $(Co{-}Fe{-}B)_x(LiNbO_{3-y})_{100-x}$ NC with $Co_zFe_{1-z}$ $(z < 0.6)$ crystal granules with possible inclusion of B atoms in them. The granules have been found to have a size about 3 nm and BCC structure with the lattice cell constant equal to $a_c = 0.29$ nm [6,7] (such granules will be referred to as Co–Fe–B). Magnetic measurements have also shown a considerable content of dispersed Fe and Co atoms in the insulating $LiNbO_{3-y}$ matrix [6–8]. High ductility of the structures (more than 256 RS states) demonstrated their high performance when used as biosimilar synapses for NCS implementation[9–11]. The found features of the M/NC/M RS structures were explained within the well-developed multifilamentary RS mechanism model [7] based on the ideas of dispersed atom nucleation around percolation nanogranule chains and formation of low-resistance filamentary nanochannels (filaments) to the $LiNbO_3$ (LNO) interface layer formed at the bottom electrode of the structures and defining their resistive state. A potentially important role of boron atoms in the achievement of high structural resistance to cyclic RS (more than $10^5$) was also noted in [6,7]. During NC synthesis, boron may fall outside the granules (owing to high diffusion mobility and high reactivity of boron) forming $B_2O_3$ type oxide and facilitating formation of significant number of oxygen vacancies in the $LiNbO_{3-y}$ matrix. However, this issue was not addressed in [6,7], because its solution required special samples and synchrotron investigation methods.

Comparative investigations of memristive properties of M/NC/M samples based on $(Co-Fe-B)_x(LiNbO_{3-y})_{100-x}$ and $(CoFe)_x(LiNbO_{3-y})_{100-x}$ NC produced from different $Co_{40}Fe_{40}B_{20}$-$LiNbO_3$ and $Co_{50}Fe_{50}$-$LiNbO_3$ composite targets, respectively, were carried out herein. Moreover, synchrotron methods were used to study the structural features of NC films that were synthesized on polyimide substrates in the same conditions as the M/NC/M samples. Finally, it is shown that the crystal structure of granules in both types of NC is the same indicating that the considerable portion of B atoms leaves for the insulating matrix during the NC synthesis and forms $B_2O_3$ type oxide. RS in these structures are more clearly pronounced.

## 2. Samples and study methods

The M/NC/M structures and NC films (witnesses) based on the $LiNbO_3$ matrix with different metallic Co−Fe−B or CoFe granules were produced by ion-beam sputtering from the $Co_{40}Fe_{40}B_{20}$-$LiNbO_3$ and $Co_{50}Fe_{50}$-$LiNbO_3$ composite targets, respectively (for details see [6,7]). It should be noted that boron is well known as an amorphizer for CoFe alloy. In particular, when about $\approx 20$ at.% of boron is contained in the (CoFe)-B cast alloy, thin $Co_{40}Fe_{40}B_{20}$ films obtained by its sputtering are amorphous with their „metallic" properties maintained [12,13].

Elongated rectangular composite targets made from $Co_{40}Fe_{40}B_{20}$ and $Co_{50}Fe_{50}$ cast alloy $(280\times80\times15\,\mathrm{mm}^3)$ plates with 16 $10\times80\,\mathrm{mm}^2$ $LiNbO_3$ bars unevenly arranged on them were used. NC was deposited in similar conditions on $60\times48\,\mathrm{mm}^2$ polyimide (kapton) and polycrystalline glass substrates at room temperature. The polycrystalline glass substrates were previously coated with a $\approx 1$ mkm three-layer metallic Cr/Cu/Cr film that serves as the bottom electrode. Uneven arrangement of accurately weighed portions of $LiNbO_3$ on the surface of the composite targets allowed to form NC in a single cycle with various metallic phase proportions within $x \approx 10-20$ at.% along the long side of the substrates (60 mm).

NC deposition rate was 15 nm/min. Witness samples on kapton substrates (for investigation of structural features of NC using the synchrotron radiation source) were deposited during 270 min (NC film thickness $d$ was $\approx 4$ mkm).

In case of M/NC/M capacitor structures, the NC layer thickness is $d \approx 0.45$ mkm. NC was deposited through a shadow mask with regularly spaced 5 mm openings. After that, $0.5\times0.2\,\mathrm{mm}^2$ top electrodes were formed (also through the shadow mask) from the Cr/Cu/Cr film.

The elemental composition of NC was measured by the energy-dispersive X-ray microanalysis (EXM) using Oxford INCA Energy 250 add-on module on JEOL JSM-6380 LV scanning election microscope. It should be noted that introduction of an unambiguous determination of $x$ is not possible in our case, because the existing EXM methods cannot detect which portion of boron is included in the metallic granules during NC growth and which one is included in the oxide matrix (see [14]). Therefore, for clarity, we will use below the value of $x$ determined using the EXM data and NC formula reflecting the target composition, i. e. $(Co_{40}Fe_{40}B_{20})_x(LiNbO_3)_{100-x}$ and $(Co_{50}Fe_{50})_x(LiNbO_3)_{100-x}$ (i. e. as in [6,7,14]).

Structural features of $(Co-Fe-B)_x(LiNbO_{3-y})_{100-x}$ and $(CoFe)_x(LiNbO_{3-y})_{100-x}$ NC films were studied by the X-ray photoelectron spectroscopy (XPS) and X-ray absorption fine structure (XAFS) analysis methods. Taking into account the available electron microscopy data [6,7] on the $Co_yFe_{1-y}$ $(y < 0.6)$ granule structure, the XAFS analysis was focused on the examination of states of Co, Fe and B, atoms dispersed in the $LiNbO_{3-y}$ matric and forming possibly an oxidized granule coating. In addition, it should be noted that for the analysis of $Co_zFe_{1-z}$ $(z < 0.6)$ type compounds, concurrent simulation on two edges with separate Co−Co, Fe−Fe, Co−Fe and Fe−Co scattering paths is required. In this case, this is difficult due to low quality of spectra for Fe edge and to the fact that the Co and Fe atom charges differ by 1 and, therefore, they are hard to distinguish by the EXAFS analysis method.

XPS spectra were measured using PHOIBOS 150 hemispherical analyzer with 1486.61 eV photon excitation. For all samples, panoramic spectra were measured and showed severe carbon contamination of the sample surface caused by their long-term exposure in atmosphere. To remove the carbon contamination and to study the deep layers of NC films, the surface portion of the sample was removed by argon ions. Surface cleaning was carried out using argon ions with energy 1500 eV during 30 min, and as a result about 60 nm surface layer was removed. Panoramic spectra measurements after ionic cleaning have shown the absence of carbon traces and significant growth of peak intensity according to the chemical analysis of the samples.

To study the structural properties of NC films by the synchrotron radiation absorption methods, two $1\times0.3\,\mathrm{mm}^2$ areas with different metal content $x \approx 12$ at.% (#1) and 18.5 at.% (#2) were chosen on the plates (sufficiently strong RS effects are observed at $x \approx 18.5$ at.% in the memresistive M/NC/M samples).

XAFS spectra measurements were performed at the „Structural Materials Science" (SMS) end-station of the Kurchatov Synchrotron Radiation Source[15,16]. The spectra were measured in the transmittance mode using oxygen-filled ionization chambers and Si (111) single-crystal monochromator with („butterfly“) cutout and energy resolution about 1 eV. ionization chamber currents were measured by Keithley picoamperemeters. For measurements of the witness film samples, thickness of each sample was varied by folding the films in several layers and the thickness was adjusted experimentally such that the absorption jump logarithm on the edge would be minimum 0.3 with an absorption coefficient above the edge of max. 3. Spectra were processed using IFEFFIT software suite [17,18]. EXAFS Fourier transforms were taken with weight coefficient $kw = 2$ within the wave number ranges $k = 2-12\,\text{Å}^{-1}$ for $K$-edge of Co and within $k = 2-10\,\text{Å}^{-1}$ for $K$-edge of Fe (the range is limited due to the vicinity to the Co edge on the high energy side).

Current-voltage curves and memristive properties of the M/NC/M structures were studied using NI PXIe-4140 (National Instruments) multifunctional sourcemeter and PM5 (Cascade Microtech) analytic probe station outfitted with PSM-100 (Motic) system to ensure micrometer movement of probes. Current-voltage curves of M/NC/M structures were measured with grounded bottom electrode and linear-step scanning at the top electrode offset voltage $U$ in sequence $0 \to +U_0 \to -U_0 \to 0\,\text{V}$ ($U_0 = 5\,\text{V}$) with increment 0.1 V and duration 50 ms. The number of scanning cycles could be repeated periodically. Endurance of structures to degradation with cyclic switching was studied by successive application of 100 ms voltage pulses: $U_{set} \to U_r \to U_{res} \to U_r$, where $U_{set} = +4\,\text{V}$ is the write voltage switching the system into the low-resistance state, $U_r = 0.5\,\text{V}$ is the read voltage and $U_{res} = -4\,\text{V}$ is the reset voltage resetting the structure to its initial state ($U_{res} \approx -U_{set}$). Measurements were carried out at room temperature in a computer-aided mode using the software specially developed in the LabVIEW environment.

## 3. Results and discussion

### 3.1. X-ray absorption fine structure spectra

The local structure of metallic granules were studied by X-ray absorption spectroscopy methods. The X-ray absorption near-edge structure (XANES) spectra on $K$-edges of Fe for NC samples with CoFe and Co–Fe–B nanogranules on kapton substrates measured in two local areas # 1 ($x \approx 12$ at.%) and # 2 ($x \approx 18.5$ at.%) are shown in Figure 1. The samples demonstrate the same degree of iron oxidation (+2).

In NC samples with CoFe granules for different regions # 1 and # 2 of the film, the local iron structures have a slight difference. The XANES spectra and EXAFS transforms (Figure 2) match together. The XANES features are clearly pronounced and the second coordination sphere can be seen in the EXAFS transform. This means that the local structure of iron is well ordered.

In the samples with Co–Fe–B granules, distinctions between film regions # 1 and # 2 are more clearly pronounced and consist in more ordered local environment in plate # 1 area ($x \approx 12$ at.%): peak of the first coordination sphere is higher and the XANES features are sharper (except prepeak $1s - 5d$ whose intensity decreases). Spectra and transform feature positions are similar, i.e. no distinctions in kind of the local structure are observed.

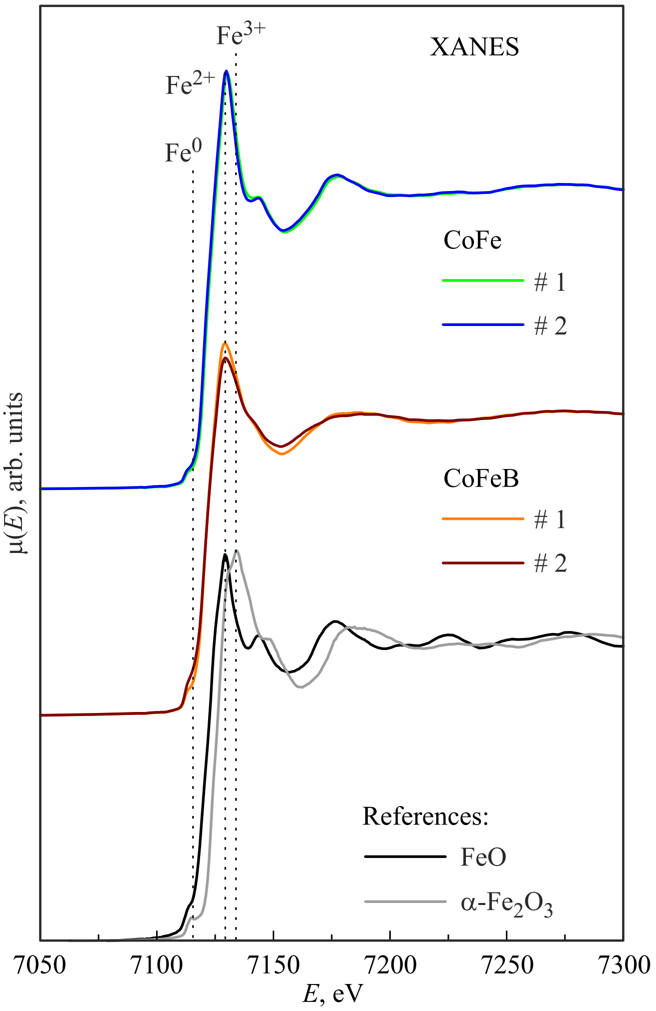

**Figure 1.** XANES spectra on $K$-edges of Fe measured in two regions # 1 and # 2 for nanocomposite samples with CoFe and Co–Fe–B granules and for FeO standard for comparison. The dashed line shows the „white line“ positions for various iron oxidation degrees.

According to the XAFS data, distinctions between the samples with CoFe and Co–Fe–B granules are in that there is a different more ordered local structure with pronounced second coordination sphere for CoFe granules than for Co–Fe–B granules, which is explained by the influence of residual boron atoms in granules whose content is, however, a priori lower than 20 at.%.

The XANES spectra were also measured on $K$-edges of Co in two regions # 1 and # 2 of NC films with CoFe and Co–Fe–B granules (Figure 3). In the samples with CoFe granules for plate regions # 1 and # 2, the local cobalt

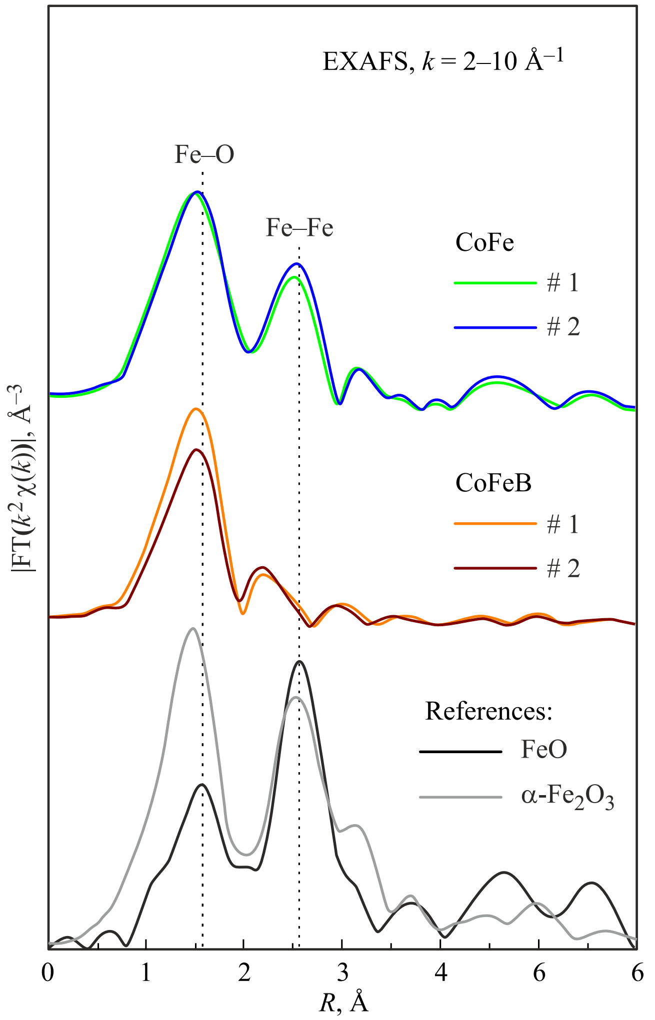

**Figure 2.** Calculated Fourier transforms of the EXAFS spectra measured on $K$-edges of Fe in two regions # 1 and # 2 for nanocomposite samples with CoFe and Co–Fe–B granules and for FeO standard for comparison.

structure differs slightly like for the Fe local structure for the XANES spectra in $K$-edge (Figure 1). The XANES spectra and EXAFS transforms (Figure 4) match together. In other words, the shape of the XANES spectra on Co and Fe in the $(CoFe)_x(LiNbO_{3-y})_{100-x}$ samples with $x \approx 12$ and 18.5 at.% is similar. This means that Co and Fe atoms have the same local and electronic structure. Two coordination spheres can be seen — oxygen sphere and another more remote sphere.

In the samples with Co–Fe–B granules, distinctions between NC film regions # 1 and # 2 are more pronounced (see Figures 3 and 4). In region # 1 ($x \approx 12$ at.%), two coordination spheres are observed. The second sphere has a smaller radius than that of the sample with CoFe granules. We suggest that this an oxygen sphere for Co with a lower oxidation degree, because, for region # 2 ($x \approx 18.5$ at.%), the sphere with the same radius as the first one. And the absorption edge is shifted to lower energies.

Fourier transform EXAFS simulation on the Co and Fe absorption edges are shown in Tables 1 and 2. For CoFe granules in region # 1, both edges are described by the structural models of oxides with cubic lattice within the interatomic distance range up to 4 Å. Scattering is observed on three coordination spheres — two oxygen spheres and one sphere populated by metal atoms. For the first sphere, the coordination number (CN) corresponds to the bulk value (6), for the second and third spheres — the coordination number is reduced, in particular for the iron edge. Thus, the local environment of iron atoms in region # 1 for NC with CoFe granules is less ordered than the cobalt environment.

For the sample with CoFe granules in region # 2, the result on the Fe edge is similar to region # 1. On the Co edge, the attempt to simulate the spectrum using only the oxide structure results in higher residual values (2% and higher). The maximum separation of the simulated and

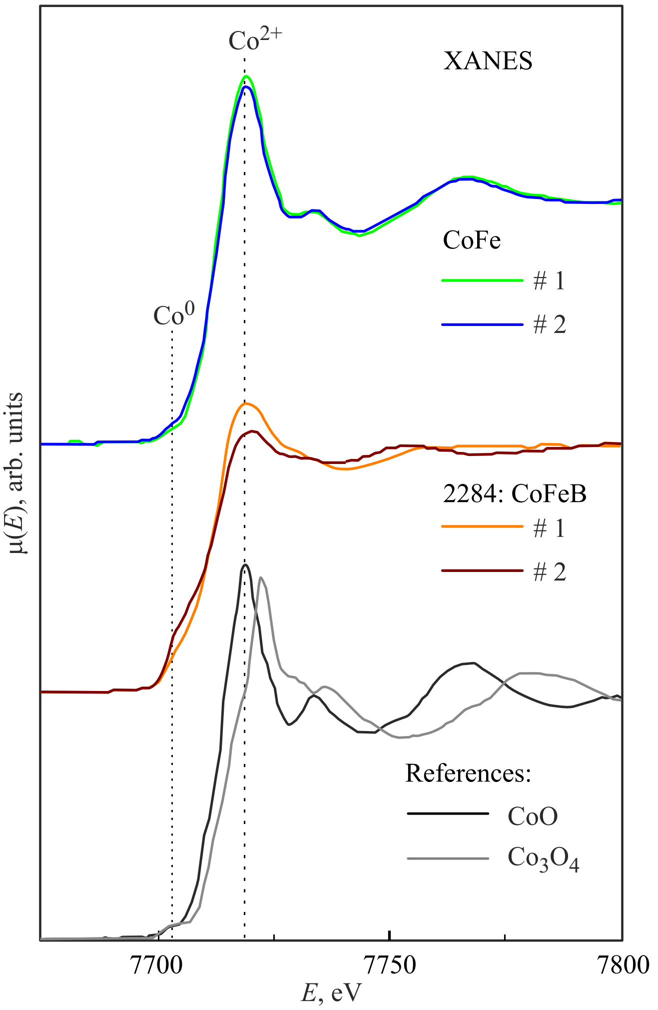

**Figure 3.** XANES spectra on $K$-edges of Co measured in two regions # 1 and # 2 for nanocomposite samples with CoFe and Co–Fe–B granules and for CoO standard for comparison. The dashed line shows the „white line“ positions for various cobalt oxidation degrees.

**Table 1.** Simulation of the EXAFS spectra on $K$-edge of Fe within $R = 1-4$ Å (NC with CoFe granules) and $R = 1-3$ Å (NC with Co–Fe–B granules). (Here, $N$ is the coordination number (CN), $R$ is the interatomic distance, $\sigma^2$ is the Debye factor, $R_f$ is the residual ($R$-factor).

| Sample | scattering path | $N$ | $R$, Å | $\sigma^2$, Å$^2$ | $R_f$, % |
|---|---|---|---|---|---|
| CoFe #1 | Fe–O | $6.0 \pm 1.0$ | $2.03 \pm 0.01$ | 0.0125 | 1.9 |
| | Fe–Fe | $4.7 \pm 1.5$ | $2.99 \pm 0.01$ | 0.0125 | |
| | Fe–O | $5.5 \pm 2.1$ | $3.67 \pm 0.04$ | 0.0125 | |
| CoFe #2 | Fe–O | $6.0 \pm 1.0$ | $2.04 \pm 0.01$ | 0.0122 | 1.3 |
| | Fe–Fe | $5.8 \pm 1.4$ | $3.00 \pm 0.01$ | 0.0134 | |
| | Fe–O | $5.5 \pm 1.6$ | $3.67 \pm 0.03$ | 0.0122 | |
| Co–Fe–B #1 | Fe–O | $3.8 \pm 0.4$ | $1.99 \pm 0.01$ | 0.0052 | 0.9 |
| | Fe–Fe | $0.3 \pm 0.4$ | $2.60 \pm 0.06$ | 0.0019 | |
| Co–Fe–B #2 | Fe–O | $4.1 \pm 0.4$ | $2.00 \pm 0.01$ | 0.0062 | 1.5 |
| | Fe–Fe | $0.5 \pm 0.4$ | $2.59 \pm 0.02$ | 0.0059 | |

**Table 2.** Simulation of the EXAFS spectra on $K$-edge of Co within $R = 1-4$ Å (NC with CoFe granules) and $R = 1-3$ Å (NC with Co–Fe–B granules)

| Sample | scattering path | $N$ | $R$, Å | $\sigma^2$, Å$^2$ | $R_f$, % |
|---|---|---|---|---|---|
| CoFe #1 | Co–O | $6.0 \pm 1.0$ | $2.04\pm$ | 0.0083 | 1.3 |
| | Co–Co | $7.3 \pm 2.7$ | $2.99\pm$ | 0.0159 | |
| | Co–O | $8.0 \pm 2.5$ | $3.61\pm$ | 0.0159 | |
| CoFe #2 | Co–O | $6.0 \pm 1.0$ | $2.03 \pm 0.01$ | 0.0077 | 0.9 |
| | Co–Co | $11.9 \pm 7.0$ | $2.98 \pm 0.03$ | 0.0150 | |
| | Co–O | $7.8 \pm 5.1$ | $3.58 \pm 0.09$ | 0.0150 | |
| | Co–Co | $0.5 \pm 1.5$ | $2.56 \pm 0.09$ | 0.0033 | |
| Co–Fe–B #1 | Co–O | $6.0 \pm 1.0$ | $1.99 \pm 0.03$ | 0.0063 | 1.0 |
| | Co–Co | $7.0 \pm 2.4$ | $2.40 \pm 0.03$ | 0.0125 | |
| Co–Fe–B #2 | Co–O | $1.7 \pm 1.2$ | $1.96 \pm 0.06$ | 0.0066 | 0.9 |
| | Co–Co | $5.6 \pm 1.6$ | $2.39 \pm 0.02$ | 0.0115 | |

experimental curves is observed in 2–3 Å region where the peaks of the first coordination sphere of metals are located. Additional „metal-metal“ scattering path introduced in the model reduces the residual significantly, but results in higher parameter determination errors. For the „metal-metal“ coordination number, the error exceeds the number itself. Thus, for the sample with CoFe granules in region #2, EXAFS indicates partial reduction of cobalt outside the granules, but this cannot be confirmed due to insufficient accuracy of the particular CN.

For the film with Co–Fe–B granules, we suggest reduction of Co (full or partial) in the $LiNbO_{3-y}$ matrix and granule coating and local Fe structure disordering that can be also followed by partial reduction. Therefore we used two scattering paths on both absorption edges — „metal-oxygen“ and „metal-metal“. For $K$-edge of Co, the simulation results agree with the qualitative analysis of the EXAFS data: the oxygen CN decreases and the metallic CN increases up to the values close to the bulk value ($N_{\text{bulk}} = 8$) meaning that large metal particles are formed. Nevertheless, even in region #2, the oxygen CN is non-zero, i.e. full reduction of cobalt does not occur outside the granules. For the iron edge, the peak corresponding to the metallic coordination sphere is not observed visually, but Fe-Fe CNs

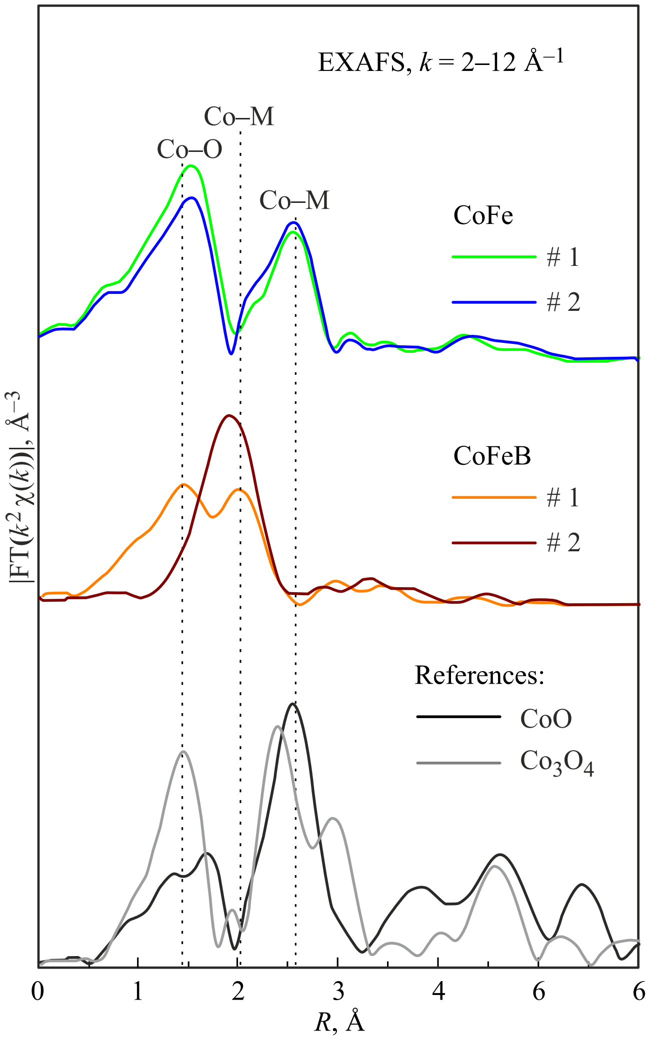

**Figure 4.** Calculated Fourier transforms of the EXAFS spectra measured on $K$-edges of Co in two regions #1 and #2 for nanocomposite samples with CoFe and Co—Fe—B granules and for CoO standard for comparison.

for both regions (#1 and #2) are non-zero, moreover, to region #2, CN exceeds the particular error. This means that in region #2 of the $(\mathrm{Co{-}Fe{-}B})_x(\mathrm{LiNbO}_{3-y})_{100-x}$ NC samples, not only cobalt, but also a small portion of iron is reduced outside the Co—Fe—B granules.

Thus, according to the EXAFS data, in both regions of the $(\mathrm{CoFe})_x(\mathrm{LiNbO}_{3-y})_{100-x}$ sample, iron outside the granules is in the form of nanoscale oxide, though in region #2, the oxide structure is less ordered. The same is also true for the local environment of cobalt. In addition, in region #2, reduction of a small portion of Co to metal is excluded. Formation of oxidized coating on CoFe granules probably causes such behavior of Fe and Co atoms.

For the $(\mathrm{Co{-}Fe{-}B})_x(\mathrm{LiNbO}_{3-y})_{100-x}$ sample, iron is in oxygen environment, but its local structure is highly disordered compared with NC for CoFe granules. Whereby, partial reduction of iron is not excluded (in region #2 — it is confirmed). Cobalt is reduced to metal — in region #1 partially, in region #2 almost completely.

**Table 3.** Concentration of chemical elements in the $(\mathrm{Co{-}Fe{-}B})_x(\mathrm{LiNbO}_{3-y})_100-x$

| Sample | name of peak | Bond energy, eV | Mass concentration, % |
|---|---|---|---|
| $(\mathrm{Co{-}Fe{-}B})_x(\mathrm{LiNbO}_{3-y})_{100-x}$ | O 1s | 531.20 | 14.386 |
| | Co2p | 778.50 | 22.889 |
| | Nb3d | 208.00 | 41.864 |
| | Fe2p | 707.20 | 18.197 |
| | B1s | 192.65 | 2.663 |

## 3.2. X-ray photoelectron spectroscopy of nanocomposite films

In X-ray photoelectron spectra of the $(\mathrm{Co{-}Fe{-}B})_x(\mathrm{LiNbO}_{3-y})_{100-x}$ and $(\mathrm{CoFe})_x(\mathrm{LiNbO}_{3-y})_{100-x}$ NC samples after ion etching, peak corresponding to the main chemical components of the test samples are observed as shown in Figure 5 and Table 3.

For the test samples, fine structure of Co2p, Nb3d, Fe2p, O1s and B1s lines was also measured to enable the valence of chemical elements to be determined by the chemical shift of the spectra. Cobalt, iron and oxygen spectra in terms of peak shapes and positions meet the reported data for $\mathrm{LiNbO_3}$ and CoFeB type compounds. In addition, in the $(\mathrm{Co{-}Fe{-}B})_x(\mathrm{LiNbO}_{3-y})_{100-x}$ NC, about 87% of boron atoms get into the insulating matrix forming the $\mathrm{B_2O_3}$ type compound, therefore, a separate intense peak occur in B1s

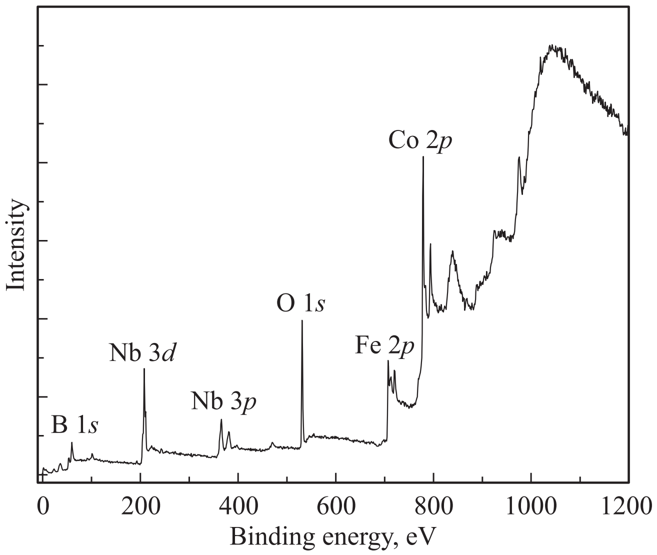

**Figure 5.** Panoramic photoelectron spectrum of the film $(\mathrm{Co{-}Fe{-}B})_x(\mathrm{LiNbO}_{3-y})_{100-x}$ NC after ionic surface cleaning.

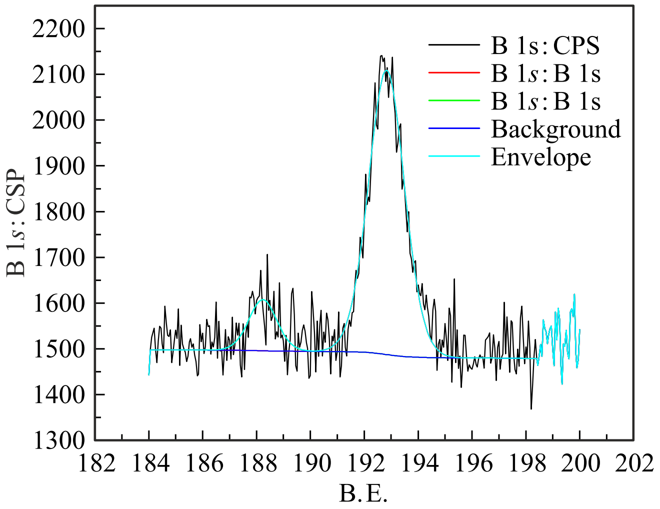

**Figure 6.** Spectrum B 1$s$ of the $(\mathrm{Co{-}Fe{-}B})_x(\mathrm{LiNbO}_{3-y})_{100-x}$ nanocomposite film after ionic surface cleaning.

spectrum at 193 eV as shown in Figure 6. This means that from 20 at.% of boron atoms only a small portion ($\approx 2.6$ at.% $= 0.13 \times 0.2$) is included in the granules during $\mathrm{Co_{40}Fe_{40}B_{20}}$ sputtering, and the rest atoms get into the $\mathrm{LiNbO}_{3-y}$ matrix, that agrees qualitatively with the XANES experiment conclusions. Therefore, the oxygen vacancy content ($y$) in the $(\mathrm{Co{-}Fe{-}B})_x(\mathrm{LiNbO}_{3-y})_{100-x}$ film matrix is much higher than that of the $(\mathrm{CoFe})_x(\mathrm{LiNbO}_{3-y})_{100-x}$ film.

### 3.3. Resistive switching of nanocomposite structures

Now let's consider the resistive switching (RS) effects in the M/NC/M structures based on the $(\mathrm{CoFe})_x(\mathrm{LiNbO}_{3-y})_{100-x}$ and $(\mathrm{Co{-}Fe{-}B})_x(\mathrm{LiNbO}_{3-y})_{100-x}$ NC containing $x \approx 12$ and 18.5 at.% of metallic phase in NC. The M/NC/M structures feature high dependence of their current-voltage curve shape on the NC composition, i.e. the metallic phase content [6]. Current-voltage curves for the M/NC/M structures with $x \approx 12$ and 18.5 at.% obtained with current limited to 50 mA are shown in Figure 7. It can be seen that the current-voltage curve hysteresis typical for the RS effect is most clearly pronounced for the $(\mathrm{Co{-}Fe{-}B})_x(\mathrm{LiNbO}_{3-y})_{100-x}$Nc based structures with $x \approx 18.5$ at.% (Figure 7, $a$). High-resistance state resistance vs. low-resistance state resistance $R_{off}/R_{on} \approx 10$ at read voltage $U \approx 0.5\,V$. At $x \approx 12$ at.% for this structure, the hysteresis loop is elongated indicating a weaker RS effect.

The M/NC/M structures based on the $(\mathrm{Co{-}Fe{-}B})_x(\mathrm{LiNbO}_{3-y})_{100-x}$ NC unlike the $\mathrm{M}/(\mathrm{CoFe})_x(\mathrm{LiNbO}_{3-y})_{100-x}/\mathrm{M}$ structures have been found to be also rather degradation-endurant during cyclic switching. Our experiments have demonstrated more than $10^4$ write/reset cycles with $R_{off}/R_{on} \approx 10$ (Figure 8).

## 4. Conclusion

Thus, the described X-ray absorption fine structure (XAFS) spectra examinations clearly show that the crystalline structure of the nanogranule oxide coating is identical in both types of the test $(\mathrm{CoFe})_x(\mathrm{LiNbO}_{3-y})_{100-x}$ and $(\mathrm{Co{-}Fe{-}B})_x(\mathrm{LiNbO}_{3-y})_{100-x}$ NC. Taking into the strong amorphizing properties of the impurity B for CoFe alloys, this suggests low content of boron in the Co–Fe–B granules compared with the boron content in the sputtered $\mathrm{Co_{40}Fe_{40}B_{20}}$-$\mathrm{LiNbO_3}$ target during NC synthesis.

Distinctions in the local structures of Fe and Co atoms that are outside the granules in the NC of interest are explained by the fact that, when $(\mathrm{Co{-}Fe{-}B})_x(\mathrm{LiNbO}_{3-y})_{100-x}$ NC is deposited, high con-

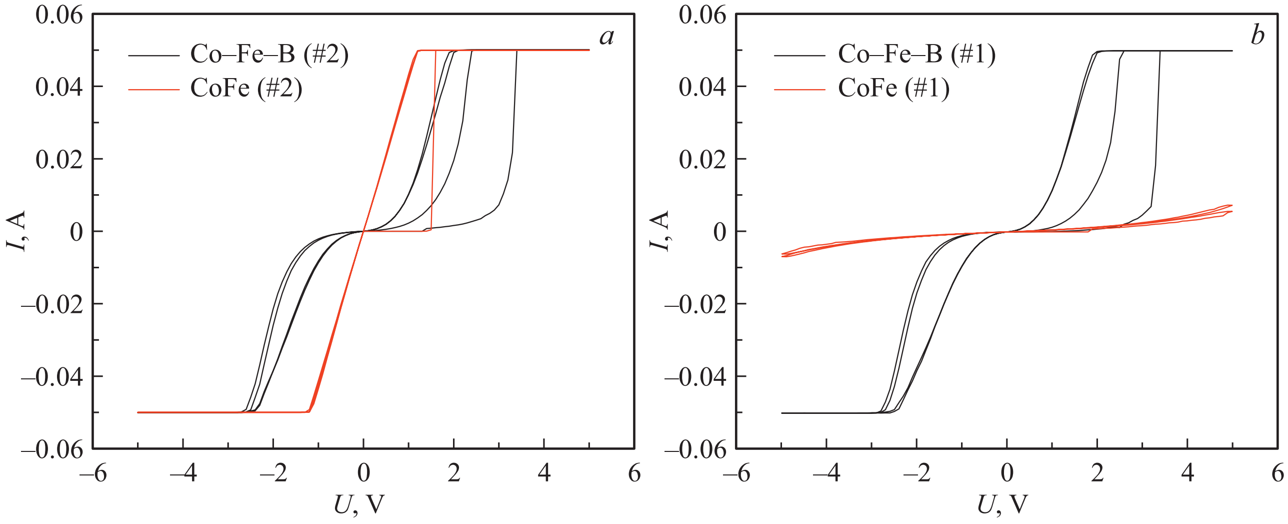

**Figure 7.** Current-voltage curves of the $\mathrm{M}/(\mathrm{CoFe})_x(\mathrm{LiNbO}_{3-y})_{100-x}/\mathrm{M}$ (red lines) and $\mathrm{M}/(\mathrm{Co{-}Fe{-}B})_x(\mathrm{LiNbO}_{3-y})_{100-x}/\mathrm{M}$ (black lines) structures with the metallic phase content $x = 18.5$ at.% ($a$) and $x = 12$ at.% ($b$).

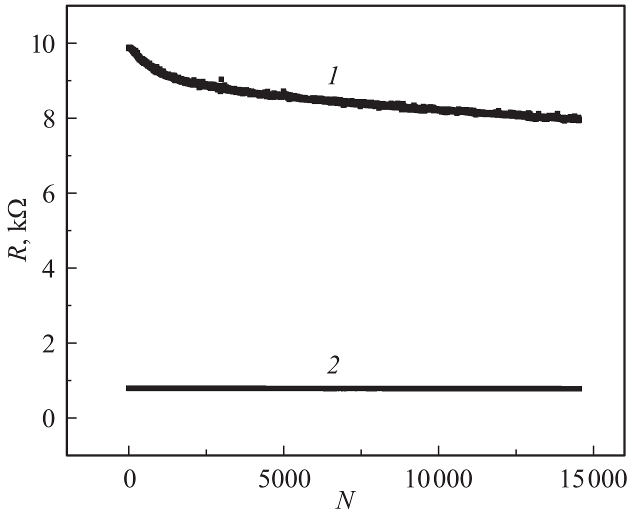

**Figure 8.** Resistance $R$ in high-resistance (*1*) and low-resistance (*2*) states vs. the number of write/reset cycles $N$ for the $M/(Co{-}Fe{-}B)_x(LiNbO_{3-y})_{100-x}/M$ structure with $x = 18.5$ at.%.

centrations of boron atoms having high diffusion mobility and high reactivity occur in the $LiNbO_{3-y}$ matrix in the form of $B_2O_3$. Moreover, excess oxygen during the synthesis of $(CoFe)_x(LiNbO_{3-y})_{100-x}$ NC will be much higher than for $(Co{-}Fe{-}B)_x(LiNbO_{3-y})_{100-x}$ NC and, therefore, a higher degree of oxidation of the Fe and Co atoms will be achieved in this case.

X-ray photoelectron spectroscopy data confirm this conclusion showing that a large portion of boron (about 87 at.%) is outside the granules in oxidized state. This results in much higher content of oxygen vacancies for $(Co{-}Fe{-}B)_x(LiNbO_{3-y})_{100-x}$ NC, facilitating vivid and stable manifestations of the RS effect in the M/NC/M structures based on this composite.

## Funding

X-ray absorption spectra were measured using Unique Research Facility „Kurchatov Synchrotron Radiation Source“. This study was funded by the Ministry of Science and Higher Education of the Russian Federation under Agreement No. 075-15-2023-324.

## Conflict of interest

The authors declare that they have no conflict of interest.

## References

[1] Z. Wang, H. Wu, G.W. Burr, C.S. Hwang, K.L. Wang, Q. Xia, J.J. Yang. Nature Rev. Mater. **5**, 173 (2020).

[2] F. Zahoor, T.Z. Azni Zulkifli, F.A. Khanday. Nanoscale Res. Lett. **15**, 90 (2020).

[3] W. Huang, X. Xia, C. Zhu, P. Steichen, W. Quan, W. i Mao, J. Yang, L. Chu, X. Li. Nano-Micro Lett. **13**, 85 (2021).

[4] M. Lanza1, A. Sebastian, W.D. Lu, M.L. Gallo, M.-F. Chang, D. Akinwande, F.M. Puglisi, H.N. Alshareef, M. Liu, J.B. Roldan. Science **376**, 1066 (2022).

[5] Q. Xia, J.J. Yang. Nature Mater. **18**, 309 (2019).

[6] V.V. Rylkov, S.N. Nikolaev, V.A. Demin, A.V. Emelyanov, A.V. Sitnikov, K.E. Nikiruy, V.A. Levanov, M.Yu. Presnyakov, A.N. Taldenkov, A.L. Vasil’ev, K.Yu. Chernoglazov, A.S. Vedeneev, Yu.E. Kalinin, A.B. Granovsky, V.V. Tugushev, A.S. Bugaev. ZhETF **153**, 424 (2018). (in Russian).

[7] M.N. Martyshov, A.V. Emelyanov, V.A. Demin, K.E. Nikiruy, A.A. Minnekhanov, S.N. Nikolaev, A.N. Taldenkov, A.V. Ovcharov, M.Yu. Presnyakov, A.V. Sitnikov, A.L. Vasiliev, P.A. Forsh, A.B. Granovskiy, P.K. Kashkarov, M.V. Kovalchuk, V.V. Rylkov. Phys. Rev. Appl. **14**, 034016 (2020).

[8] V.V. Rylkov, A.V. Emelyanov, S.N. Nikolaev, K.E. Nikiruy, A.V. Sitnikov, E.A. Fadeev, V.A. Demin, A.B. Granovsky. ZhETF **158**, 164 (2020). (in Russian).

[9] A.V. Emelyanov, K.E. Nikiruy, A.V. Serenko, A.V. Sitnikov, M.Yu. Presnyakov, R.B. Rybka, A.G. Sboev, V.V. Rylkov, P.K. Kashkarov, M.V. Kovalchuk, V.A. Demin. Nanotechnology **31**, 045201 (2020).

[10] V.A. Demin, D.V. Nekhaev, I.A. Surazhevsky, K.E. Nikiruy, A.V. Emelyanov, S.N. Nikolaev, V.V. Rylkov, M.V. Kovalchuk. Neural Networks **134**, 64 (2021).

[11] A.N. Matsukatova, A.I. Ilyasov, K.E. Nikiruy, E.V. Kukueva, A.L. Vasiliev, B.V. Goncharov, A.V. Sitnikov, M.L. Zanaveskin, A.S. Bugaev, V.A. Demin, V.V. Rylkov, A.V. Emelyanov. Nanomaterials **12**, 3455 (2022).

[12] Y.-T. Chen and S.M. Xie. J. Nanomater. 2012, 486284( 2012).

[13] G.V. Swamy, H. Pandey, A.K. Srivastava, M.K. Dalai, K.K. Maurya, Rashmi, R.K. Rakshit. AIP Adv. **3**, 072129 (2013).

[14] V.V. Rylkov, S.N. Nikolaev, K.Yu. Chernoglazov, V.A. Demin, A.V. Sitnikov, M.Yu. Presnyakov, A.L. Vasiliev, N.S. Perov, A.S. Vedeneev, Yu.E. Kalinin, V.V. Tugushev, A.B. Granovsky. Phys. Rev. B **95**, 144202 (2017).

[15] A. Chernyshov, A. Veligzhanin, Y. Zubavichus. Nucl. Instr. Meth. Phys. Res. A. **603**, 95 (2009).

[16] N. Trofimova, A. Veligzhanin, V. Murzin, A. Chernyshov, E. Khramov, V. Zabluda, I. Edel’man, Y. Slovokhotov, Y. Zubavichus. Ross. Nanotechnol. **8**, 396 (2013).

[17] B. Ravel. J. Synchrotron. Rad. **12**, 537 (2005).

[18] M. Newille. J. Synchrotron. Rad. **8**, 322 (2001).

*Translated by E.Ilyinskaya*